Quantum nonreciprocal switching effect in a triple-quantum-dot structure

Jia-Rui Li[1], Cui Jiang[2], and Wei-Jiang Gong[1]*
[1] *College of Sciences, Northeastern University, Shenyang 110819, China*
[2] *College of Sciences, Shenyang Institute of Engineering, Shenyang 110036, China*
(Dated: August 30, 2026)

We investigate the eigenenergy spectra and quantum transport of a triple-quantum-dot (TQD) system with nonreciprocal couplings ($t_c \pm \gamma$) between the two side dots. For the magnetic-flux phase factor $\phi = n\pi$, parity-time ($\mathcal{PT}$) symmetry breaking occurs as γ increases, and a smaller γ favors the formation of the exceptional point (EP) when the side dots are weakly coupled to the main-channel dot. Notably, this weak coupling induces a higher-order EP when $\phi \neq n\pi$. Nonreciprocal couplings also modulate the Fano lineshape of the transmission spectrum in a nontrivial manner: besides shifting the lineshapes, they induce Fano deformation when γ satisfies the EP condition. More interestingly, when the couplings between the main-channel dot and the side dots are detuned, nonreciprocal couplings trigger a bound state in the continuum (BIC) and a reversal of the Fano lineshape, both of which become more pronounced as the detuning increases. Our results reveal the distinctive role of nonreciprocal couplings in regulating quantum transport in a TQD structure.

I. INTRODUCTION

Non-Hermitian systems refer to open systems that can be described by non-Hermitian Hamiltonians. In the early stages of quantum theory, non-Hermitian Hamiltonians were once deemed unphysical because of their complex eigenvalues and the apparent violation of unitary time evolution. In 1998, however, Bender and Boettcher showed that non-Hermitian Hamiltonians possessing parity-time ($\mathcal{PT}$) symmetry can still exhibit purely real spectra [1], which established the physical validity of this class of systems. At present, non-Hermitian systems are realized mainly in two ways. The first is to introduce gain-loss imaginary potentials [2–5]. In such systems, imaginary potentials have been shown to regulate $\mathcal{PT}$-symmetry phase transitions [6, 7], exceptional points [8], and other phenomena that are unique to non-Hermitian physics. These systems also hold promising applications in quantum simulation, photonics, quantum heat engines, and topological photonics [9–12].

The second realization relies on nonreciprocal couplings [13–17]. In nonreciprocal systems, asymmetric hopping amplitudes break the conventional bulk-boundary correspondence and give rise to the non-Hermitian skin effect [18–20]. This effect has stimulated extensive studies of non-Bloch band theory, including the generalized Brillouin zone, non-Bloch topological invariants, and saddle-point methods [21–25]. Based on the bulk skin localization and the properties of edge states, the skin-topological effect was subsequently identified. Experimentally, the non-Hermitian skin effect has been observed in topolectrical circuits [26–28], photonic lattices [29], and ultracold Fermi gases [30]. These advances not only deepen the understanding of non-Hermitian systems but also provide a theoretical basis for designing novel functional devices.

With the development of non-Hermitian quantum physics, its implications for quantum transport in one-dimensional systems have attracted growing interest [31–34]. In Fano-Anderson systems, $\mathcal{PT}$-symmetric potentials can induce transitions from perfect reflection to perfect transmission and govern perfect reflection at single or dual resonant frequencies [35]. In non-Hermitian Aharonov-Bohm rings with one quantum dot (QD) embedded in each arm, the conductance spectrum exhibits an asymmetric Fano profile under appropriate conditions, purely as a consequence of the non-Hermiticity [36, 37]. Similarly, rhombic QD rings with $\mathcal{PT}$ symmetry support reciprocal reflection (transmission) and unidirectional transmission (reflection) at the axial (reflection) $\mathcal{PT}$-symmetric ring center [38]. More recently, stable Bloch oscillations and Landau-Zener tunneling have been reported in a non-Hermitian $\mathcal{PT}$-symmetric flat-band lattice [39], and non-Hermitian mechanisms have been shown to induce the anomalous Hall effect [40]. These works demonstrate that $\mathcal{PT}$ symmetry plays a pivotal role in shaping quantum transport.

It should be emphasized that all of the above transport effects stem from the modification of quantum interference by non-Hermitian factors. It is therefore natural to ask how a different non-Hermitian ingredient, namely nonreciprocal coupling, modifies quantum transport. So far, transport studies of nonreciprocity have mainly focused on asymmetric system-reservoir couplings (i.e., $\Gamma_L \neq \Gamma_R$ or complex self-energies) [41], which endow forward- and backward-propagating electrons with unequal lifetimes and produce a point-gap spectral topology. The role of nonreciprocal *interdot* couplings [42, 43] in quantum transport has received only limited attention [44, 45]: existing works concentrate on nonreciprocity-induced unidirectional transparency, whereas the interplay among nonreciprocal couplings, exceptional-point physics, and Fano interference in few-QD systems remains largely unexplored. In particular, neither the condition under which a nonreciprocal coupling generates higher-order EPs in a small QD cluster nor the transport

*Electronic address: gwj@neu.edu.cn

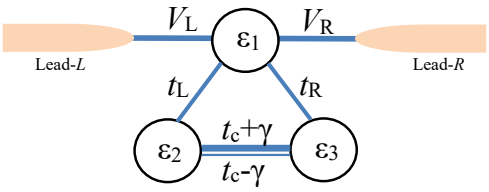


FIG. 1: Schematic of the non-Hermitian TQD system coupled to the left and right leads (lead-L, lead-R). The system consists of three single-level QDs with levels ε_1, ε_2, and ε_3. t_L and t_R denote the coupling coefficients between QD-1 and QD-2 (QD-3), respectively, whereas $t_c+\gamma$ and $t_c-\gamma$ denote the nonreciprocal couplings between QD-2 and QD-3. V_L and V_R are the tunneling couplings between QD-1 and the left and right leads.

signatures of such EPs has been clarified.

In the present work, we address these issues by studying the eigenenergies of a triple-quantum-dot (TQD) system with nonreciprocal couplings ($t_c\pm\gamma$) between the two side QDs, together with their signatures in the quantum transport spectra. We find that for the magnetic-flux phase factor $\phi = n\pi$, $\mathcal{PT}$-symmetry breaking arises with increasing γ, and that a smaller γ favors the formation of an exceptional point (EP) when the side QDs are weakly coupled to the main-channel QD. Notably, such weak coupling induces a higher-order EP at $\phi \neq n\pi$. The nonreciprocal couplings also modulate the Fano lineshape of the transmission spectrum in a nontrivial way: in addition to shifting the lineshapes, they cause Fano deformation when γ satisfies the EP condition. More interestingly, when the couplings between the main-channel QD and the side QDs are detuned, the nonreciprocal couplings trigger a bound state in the continuum (BIC) and a reversal of the Fano lineshape, and both effects are enhanced as the detuning increases. Compared with previous studies, the breakthrough of this work is threefold: (i) we derive analytical conditions for conventional and higher-order EPs in a nonreciprocal few-QD system; (ii) we establish a direct correspondence between these EPs and the evolution of Fano lineshapes in the transmission spectrum; and (iii) we obtain a closed-form BIC condition and identify the accompanying Fano-lineshape reversal, which together provide a concrete scheme for a nonreciprocal quantum switch. Our findings clarify the unique role of nonreciprocal couplings in regulating quantum transport in TQD structures.

II. MODEL AND METHODOLOGY

Figure 1 shows a schematic of the structure that hosts the quantum nonreciprocal switching effect. The setup is effectively equivalent to a TQD system in which two leads are coupled to QD-1 simultaneously. The Hamiltonian of the system can be written as

$$H = H_{\rm w} + H_{\rm c} + H_{\rm t}. \tag{1}$$

Here $H_{\rm w}$ describes the two semi-infinite leads, $H_{\rm c}$ is the Hamiltonian of the TQD core containing the nonreciprocal coupling between QD-2 and QD-3, and $H_{\rm t}$ describes the tunneling coupling between the leads and the TQD system. The three parts are given explicitly by

$$\begin{aligned} H_{\rm w} &= \sum_{\alpha=L,R}\sum_{n=1}^{\infty} t_0 c^\dagger_{\alpha,n+1} c_{\alpha n} + \text{h.c.}, \\ H_{\rm c} &= \sum_{j=1}^{3} \varepsilon_j d_j^\dagger d_j + (t_L d_1^\dagger d_2 + t_R d_3^\dagger d_1 + \text{h.c.}) \\ &\quad + (t_c+\gamma) d_2^\dagger d_3 + (t_c-\gamma) d_3^\dagger d_2, \\ H_{\rm t} &= \sum_{\alpha} V_\alpha c^\dagger_{\alpha 1} d_1 + \text{h.c.}. \end{aligned} \tag{2}$$

In these expressions, $c^\dagger_{\alpha n}$ ($c_{\alpha n}$) denotes the creation (annihilation) operator of an electron at the n-th site of lead-α, and t_0 is the nearest-neighbor hopping amplitude in the leads. $d_j^\dagger$ (d_j) ($j = 1,2,3$) is the creation (annihilation) operator of an electron in the j-th QD, and ε_j is the corresponding QD level. Throughout this work, t_L and t_R denote the (complex) couplings between QD-1 and QD-2 (QD-3); whenever their magnitudes are equal, we abbreviate them as $|t_\alpha| \equiv |t_L| = |t_R|$ with $\alpha = L, R$, and otherwise we write $|t_L|$ and $|t_R|$ explicitly. The parameters $t_c+\gamma$ and $t_c-\gamma$ are the nonreciprocal interdot coupling amplitudes between QD-2 and QD-3, where t_c is the symmetric (reciprocal) part and γ is the nonreciprocal coupling strength that quantifies the breaking of reciprocity. Because the three QDs form a closed ring, the magnetic-flux phase factor plays a nontrivial role. Without loss of generality, we take $t_L = |t_L|$ and $t_R = |t_R|e^{i\phi}$, with ϕ being the flux-induced phase. V_α denotes the tunneling coupling between lead-α and QD-1. The finite nonreciprocal coupling γ is the core origin of the non-Hermitian effect in this system.

From a physical perspective, a nonreciprocal interdot coupling $t_c \pm \gamma$ can originate from several microscopic mechanisms that break both time-reversal symmetry and reciprocity, and has been realized in numerous practical systems. First, in QD rings threaded by a magnetic flux, the interplay between the flux-induced gauge phase and inelastic or dissipative interdot processes generates direction-dependent tunneling, so that the clockwise and anticlockwise hopping amplitudes differ by 2γ [42, 46, 47]. Second, reservoir engineering provides a generic route: when two sites are coupled not only coherently but also dissipatively through a common structured reservoir, the interference between the coherent and dissipative channels yields an effective nonreciprocal coupling, whose magnitude γ is controlled by the relative phase of the two channels [48, 49]. Third, periodic (Floquet) modulation of the interdot tunneling barrier produces, within

the rotating-wave approximation, an effective nonreciprocal hopping whose strength and direction are tuned by the modulation phase difference [50]. Finally, the same non-Hermitian core can be emulated in classical platforms: in topolectrical circuits, asymmetric admittance coupling between two nodes is realized with impedance-negative converters or asymmetric LC elements [51–55], and in photonic or cold-atom settings, artificial gauge fields generate asymmetric couplings [46, 47]. Our TQD structure can thus be mapped directly onto a three-node non-Hermitian circuit or a modulated QD ring, which makes the present model experimentally accessible.

To investigate the transmission properties of the proposed TQD system, we adopt the transfer-matrix method to derive the analytical expression for the transmission amplitude. The key steps are outlined as follows. The total wave function of the system is expanded in terms of the states of the quantum wires and the QDs, $|\psi\rangle = \sum_{\alpha n} c_{\alpha n}(t)|\phi_{\alpha n}\rangle + \sum_{j=1}^{3} d_j(t)|\varphi_j\rangle$, where $|\phi_{\alpha n}\rangle = c_{\alpha n}^{\dagger}|0\rangle$ and $|\varphi_j\rangle = d_j^{\dagger}|0\rangle$ are the states of the wire sites and the QDs, respectively. Substituting this expansion into the time-dependent Schrödinger equation $i\partial_t|\psi\rangle = H|\psi\rangle$, we obtain the coupled-mode equations

$$\begin{aligned} i\dot{c}_{\alpha n} &= t_0 c_{\alpha,n-1}(1-\delta_{n1}) + t_0 c_{\alpha,n+1} + V_\alpha d_1 \delta_{n1}, \\ i\dot{d}_1 &= \varepsilon_1 d_1 + t_L d_2 + t_R^* d_3 + \sum_\alpha V_\alpha^* c_{\alpha 1}, \\ i\dot{d}_2 &= \varepsilon_2 d_2 + t_L^* d_1 + (t_c+\gamma) d_3, \\ i\dot{d}_3 &= \varepsilon_3 d_3 + t_R d_1 + (t_c-\gamma) d_2. \end{aligned} \tag{3}$$

For simplicity, t_0 is taken to be a real constant. We then consider the stationary solutions $c_{\alpha n}(t) = A_{\alpha n} e^{-i\omega t}$ and $d_j(t) = B_j e^{-i\omega t}$, where ω is the energy of the incident electron. Substitution into Eq. (3) yields the algebraic relations

$$\begin{aligned} \omega A_{\alpha n} &= t_0 A_{\alpha,n-1}(1-\delta_{n1}) + t_0 A_{\alpha,n+1} + V_\alpha B_1 \delta_{n1}, \\ \omega B_1 &= \varepsilon_1 B_1 + t_L B_2 + t_R^* B_3 + \sum_\alpha V_\alpha^* A_{\alpha 1}, \\ \omega B_2 &= \varepsilon_2 B_2 + t_L^* B_1 + (t_c+\gamma) B_3, \\ \omega B_3 &= \varepsilon_3 B_3 + t_R B_1 + (t_c-\gamma) B_2. \end{aligned} \tag{4}$$

Rearranging the equations for the TQD amplitudes B_1, B_2, and B_3, we rewrite them in matrix form,

$$M \begin{bmatrix} B_1 \\ B_2 \\ B_3 \end{bmatrix} = \begin{bmatrix} \sum_\alpha V_\alpha^* A_{\alpha 1} \\ 0 \\ 0 \end{bmatrix}, \tag{5}$$

where the 3×3 coefficient matrix is

$$M = \begin{bmatrix} \omega - \varepsilon_1 & -t_L & -t_R^* \\ -t_L^* & \omega - \varepsilon_2 & -(t_c+\gamma) \\ -t_R & -(t_c-\gamma) & \omega - \varepsilon_3 \end{bmatrix}. \tag{6}$$

Solving Eq. (5) with Cramer's rule, we express the amplitude B_1 of QD-1, which is directly coupled to the leads, in terms of the wire amplitudes $A_{\alpha 1}$:

$$B_1 = \frac{M_{11}}{\det M} \sum_\alpha V_\alpha^* A_{\alpha 1}, \tag{7}$$

where M_{11} is the algebraic cofactor of the $(1,1)$ entry of M. Substituting B_1 back into the wire equation, we obtain a renormalized equation that incorporates the self-energy induced by the side-coupled QDs,

$$\omega A_{\alpha n} = t_0 A_{\alpha,n-1}(1-\delta_{n,1}) + t_0 A_{\alpha,n+1} + \sum_{\alpha'} \mu_{\alpha\alpha'} A_{\alpha' 1} \delta_{n1}, \tag{8}$$

with the effective self-energy $\mu_{\alpha\alpha'} = \frac{M_{11}}{\det M} V_\alpha V_{\alpha'}^*$. For $n = 1$, Eq. (8) simplifies to

$$\begin{aligned} (\omega - \mu_{LL}) A_{L1} &= t_0 A_{L2} + \mu_{LR} A_{R1}, \\ (\omega - \mu_{RR}) A_{R1} &= t_0 A_{R2} + \mu_{RL} A_{L1}. \end{aligned} \tag{9}$$

To analyze the scattering, we introduce the ansatz $A_{Ln} = e^{ikn} + re^{-ikn}$ and $A_{Rn} = \tau e^{ikn}$, where k is the wave number in the leads, and r and τ are the reflection and transmission amplitudes. Substituting this ansatz into Eq. (9) yields a linear system for r and τ,

$$\begin{aligned} &\begin{bmatrix} (\omega - \mu_{LL}) - t_0 e^{ik} & -\mu_{LR} \\ -\mu_{RL} & (\omega - \mu_{RR}) - t_0 e^{ik} \end{bmatrix} \begin{bmatrix} r \\ \tau \end{bmatrix} \\ &= \begin{bmatrix} -(\omega - \mu_{LL}) + t_0 e^{-ik} \\ \mu_{RL} \end{bmatrix}. \end{aligned} \tag{10}$$

Solving this system gives the transmission amplitude

$$\tau = \frac{t_0 \mu_{RL} \left(e^{ik} - e^{-ik}\right)}{\left[(\omega - \mu_{LL}) - t_0 e^{ik}\right]\left[(\omega - \mu_{RR}) - t_0 e^{ik}\right] - \mu_{LR}\mu_{RL}}, \tag{11}$$

where $\omega = 2t_0 \cos k$. The transmission function is then given by

$$T_{LR}(\omega) = |\tau|^2. \tag{12}$$

To further explore the transport characteristics of the TQD structure, we alternatively employ the nonequilibrium Green function (NEGF) technique, which provides an intuitive picture of quantum interference in open systems. Within the NEGF framework, the transmission function between the left and right leads reads

$$T_{LR}(\omega) = \mathrm{Tr}\left[\Gamma_L(\omega) G^r(\omega) \Gamma_R(\omega) G^a(\omega)\right], \tag{13}$$

where $\Gamma_\alpha = i(\Sigma_\alpha - \Sigma_\alpha^\dagger)$ characterizes the coupling between lead-α and the TQD region. The self-energy $\Sigma_\alpha = |V_\alpha|^2 g_s$ is induced by the coupling between the TQDs and lead-α, with g_s being the surface Green function of the lead. Owing to the uniform intersite coupling in the leads, g_s admits the simple analytical form $g_s = \frac{\omega}{2t_0^2} - i\rho_0$, where $\rho_0 = \frac{\sqrt{4t_0^2 - \omega^2}}{2t_0^2}$ is the density of states of the lead.

Equation (13) involves the retarded and advanced Green functions, defined by $G_{jl}^r(t) = -i\theta(t)\langle\{d_j(t), d_l^\dagger\}\rangle$

and $G^a_{jl}(t) = i\theta(-t)\langle\{d_j(t), d_l^\dagger\}\rangle$, where $\theta(x)$ is the Heaviside step function. Their Fourier transforms $G^{r(a)}_{jl}(\omega) = \int_{-\infty}^{\infty} G^{r(a)}_{jl}(t)e^{i\omega t}dt$ can be solved systematically by the equation-of-motion method. For notational simplicity, we use the shorthand $\langle\langle A|B\rangle\rangle^x$ $(x = r, a)$ for these Fourier-space Green functions, e.g., $G^r_{jl}(\omega) = \langle\langle d_j|d_l^\dagger\rangle\rangle^r$. In general, the Green functions obey

$$(\omega \pm i0^+)\langle\langle A|B\rangle\rangle^{r(a)} = \langle\{A, B\}\rangle + \langle\langle[A, H]|B\rangle\rangle^{r(a)}. \quad (14)$$

Starting from Eq. (14), we derive the equations of motion for the retarded Green functions $\langle\langle d_j|d_l^\dagger\rangle\rangle^r$ and obtain their matrix form,

$$[G^r]^{-1} = \begin{bmatrix} z-\varepsilon_1-\Sigma_L-\Sigma_R & -t_L & -t_R^* \\ -t_L^* & z-\varepsilon_2 & -(t_c+\gamma) \\ -t_R & -(t_c-\gamma) & z-\varepsilon_3 \end{bmatrix}, \quad (15)$$

with $z = \omega + i0^+$. The advanced Green function follows from $G^a = [G^r]^\dagger$. The transmission amplitude is then

$$\tau = \sqrt{\Gamma_L\Gamma_R}\, G^r_{11} = \frac{\sqrt{\Gamma_L\Gamma_R}\, M_{11}}{(z-\varepsilon_1-\Sigma_L-\Sigma_R)M_{11} - M_{12} - M_{13}}, \quad (16)$$

with $M_{11} = (\omega-\varepsilon_2)(\omega-\varepsilon_3) - (t_c^2-\gamma^2)$, $M_{12} = |t_L|^2(\omega-\varepsilon_3) + |t_R|^2(\omega-\varepsilon_2)$, and $M_{13} = t_L t_R(t_c+\gamma) + t_L^* t_R^*(t_c-\gamma)$. This result can be shown to agree exactly with Eq. (11), which confirms the reliability of our methodology.

III. NUMERICAL RESULTS AND DISCUSSIONS

Based on the formalism in Sec. II, we now calculate the transport properties of the TQD system in which the two side-coupled QDs are connected by the nonreciprocal couplings $t_c \pm \gamma$. We take t_c as the energy unit ($t_c = 1.0$) and normalize all other parameters to it. The leads are treated within the wide-band limit ($t_0 \gg \omega$), and the QD-lead coupling strength is fixed at $\Gamma_\alpha = 0.25$. The QD levels are set to $\varepsilon_j = 0$ for simplicity.

Before presenting the results, we clarify the terminology used below to describe the transmission spectra. A *Fano peak* denotes an asymmetric resonance maximum that arises from the interference between the continuum channel (the lead-QD-1-lead path) and a discrete eigenstate of the TQD core. A *Fano antiresonance* denotes the transmission zero, $T(\omega) = 0$, that accompanies a Fano peak and originates from complete destructive interference. A *transmission valley* (or dip) denotes a local minimum with finite nonzero transmission, in contrast to the exact zero of an antiresonance. Finally, *Fano-lineshape reversal* denotes the inversion of the asymmetry of a Fano profile, i.e., the exchange of the relative positions of the Fano peak and its adjacent Fano antiresonance with respect to the resonance center, which corresponds to a sign reversal of the effective Fano parameter. These terms are used consistently throughout the following discussion.

A. Eigenenergy spectra and exceptional points

Figure 2 shows the real and imaginary parts of the eigenenergies of the isolated TQD core as functions of γ. In the Hermitian limit $\gamma = 0$, the system has three discrete real eigenenergies, and all imaginary parts are strictly zero. Once the system enters the non-Hermitian regime ($\gamma \neq 0$), the three eigenenergies evolve in distinct ways.

For $\phi = 0$ (top row of Fig. 2) and $|t_\alpha| = 0.2$, the real parts of E_1 and E_2 develop a pronounced minimum and maximum, respectively, at $\gamma \approx 0.86$. Beyond this point, their imaginary parts emerge with opposite signs. This signals the formation of an EP at which the real parts of E_1 and E_2 coalesce. When $|t_\alpha|$ increases to 0.5, the EP shifts to a smaller critical value $\gamma \approx 0.56$. At $|t_\alpha| = 1.0$, the EP disappears, and the imaginary parts of E_1 and E_2 grow linearly with γ as long as γ is nonzero. Meanwhile, for $\phi = 0$, E_3 remains purely real over the whole range of γ, irrespective of the value of $|t_\alpha|$. The spectral evolution at $\phi = \pi$ (bottom row) is mirror symmetric to that at $\phi = 0$. In that case, the nonzero imaginary parts originate from E_2 and E_3, while E_1 remains purely real. This opposite-sign behavior of the imaginary parts stems from the phase-induced symmetry of the nonreciprocal couplings.

For $\phi = 0.5\pi$ (middle row of Fig. 2), the mirror symmetry of the system is broken. Nonzero imaginary parts appear as soon as γ deviates from zero, and E_2 remains a purely imaginary eigenenergy. The three $|t_\alpha|$ cases nevertheless differ from one another. For $|t_\alpha| = 0.2$, all three eigenstates coalesce at $\gamma = 1.2$, forming a higher-order EP that is clearly distinct from the conventional EPs at $\phi = 0$ and π. Within the range $\gamma \in (0, 1.2]$, the real parts of E_1 and E_3 are equal in magnitude but opposite in sign, whereas their imaginary parts are identical; the imaginary parts of E_1 and E_3 split only at the higher-order EP. For $|t_\alpha| \geq 0.5$, no EP exists. These results show that the phase factor ϕ and the tunneling amplitude $|t_\alpha|$ jointly control the emergence and the position of EPs, as well as the transition between a fully real spectrum and a complex one.

Figure 3 displays the eigenenergy evolution for the asymmetric case $|t_L| = 0.2$ with $|t_R| = 0.5$ (top row) and $|t_R| = 1.0$ (bottom row). For $|t_R| = 0.5$ and $\phi = 0$, the real parts of E_1 and E_2 coalesce at $\gamma \approx 0.8$, forming a conventional EP; beyond it, their imaginary parts emerge with opposite signs, while E_3 stays purely real. The spectrum at $\phi = \pi$ is mirror symmetric to that at $\phi = 0$, with E_2 and E_3 becoming degenerate at $\gamma \approx 0.8$ and E_1 remaining real. For $\phi = 0.5\pi$, nonzero imaginary parts appear for any finite γ, and at $\gamma = 1.4$ all three eigenstates coalesce into a higher-order EP. For $|t_R| = 1.0$, conventional EPs occur at $\gamma \approx 1.0$ for both $\phi = 0$ and $\phi = \pi$, whereas at $\phi = 0.5\pi$ all eigenenergies are complex and evolve linearly with γ, so that both conventional and higher-order EPs are eliminated. These results confirm that $|t_R|$ and ϕ jointly control the EPs: the $\phi = 0/\phi = \pi$

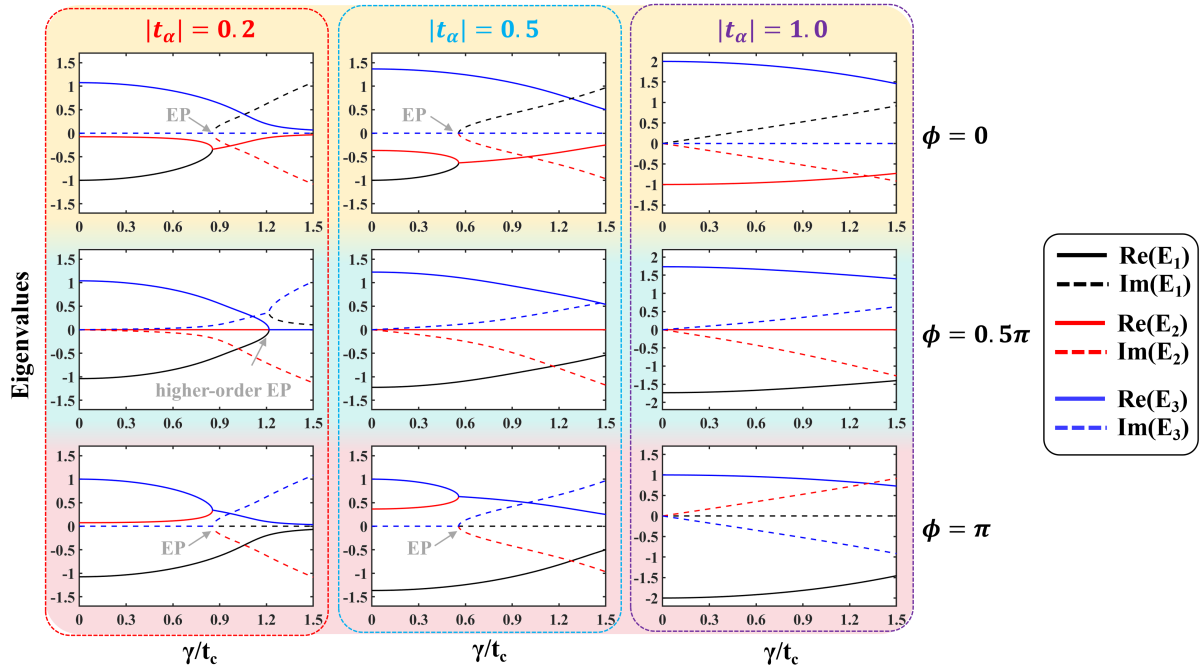


FIG. 2: Eigenenergy spectra (real and imaginary parts) of the isolated non-Hermitian TQD core as functions of the nonreciprocal coupling strength γ for different tunneling amplitudes $|t_\alpha| \equiv |t_L| = |t_R|$. The first to third columns correspond to $|t_\alpha| = 0.2$, 0.5, and 1.0, respectively. The first to third rows correspond to $\phi = 0$, 0.5π, and π, respectively. In each panel, the three eigenenergies E_1, E_2, and E_3 are shown in black, red, and blue, respectively; the real part of each eigenenergy is plotted as a solid line and its imaginary part as a dashed line of the same color.

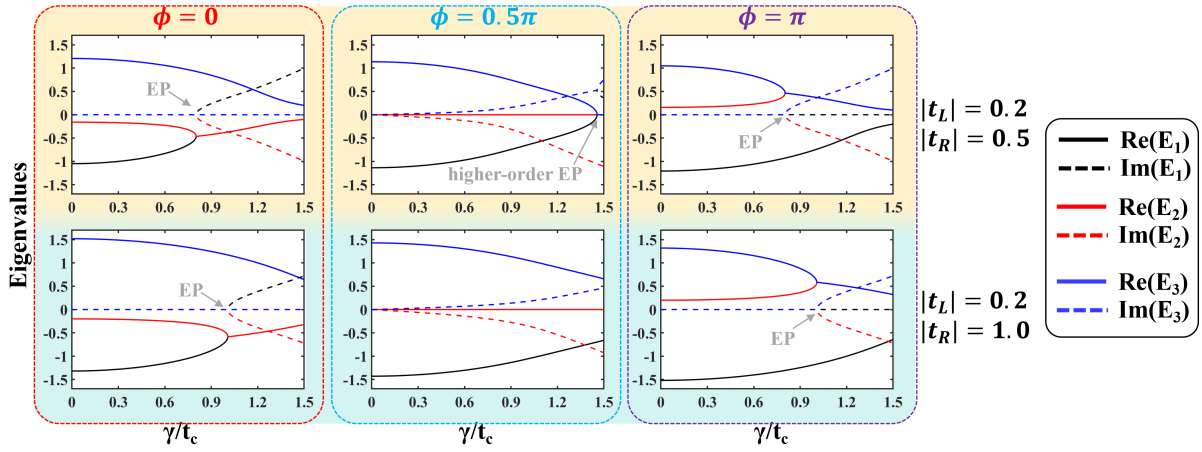


FIG. 3: Eigenenergy spectra of the TQD core as functions of γ for fixed $|t_L| = 0.2$ and two values of the right tunneling amplitude, $|t_R| = 0.5$ (top row, panels (a)–(c)) and $|t_R| = 1.0$ (bottom row, panels (d)–(f)). The phase factor is $\phi = 0$, 0.5π, and π from left to right. Color and line-style conventions are the same as in Fig. 2: E_1, E_2, and E_3 are shown in black, red, and blue, with solid (dashed) lines for the real (imaginary) parts.

symmetry produces mirrored spectra, while $\phi = 0.5\pi$ breaks this symmetry and favors a higher-order EP at small $|t_R|$.

The emergence of EPs can be understood analytically from the eigenenergy equation. For $\phi = 0$ (and $\varepsilon_j = 0$), the characteristic equation of H_c reads

$$\omega^3 - A\omega - B_r = 0, \tag{17}$$

where $A = |t_L|^2 + |t_R|^2 + t_c^2 - \gamma^2$ and $B_r = 2t_c|t_L t_R|$. The corresponding discriminant is $\Delta = \frac{B_r^2}{4} - \frac{A^3}{27}$. When $\Delta > 0$, the equation has one real root and a pair of complex-conjugate roots; when $\Delta = 0$, it has three real

roots with at least two equal; when $\Delta < 0$, it has three distinct real roots. The condition for a pair of complex-conjugate solutions, $\frac{B_r^2}{4} - \frac{A^3}{27} > 0$, therefore yields

$$27t_c^2|t_L t_R|^2 > \left(|t_L|^2 + |t_R|^2 + t_c^2 - \gamma^2\right)^3. \quad (18)$$

The transition point, i.e., the EP, is given explicitly by $\gamma_{c1} = \sqrt{|t_L|^2 + |t_R|^2 + t_c^2 - 3\left(t_c^2|t_L t_R|^2\right)^{1/3}}$. Since the discriminant is the same for $\phi = 0$ and $\phi = \pi$, the same EP appears at these two phases for identical structural parameters. To understand this result, we analyze the symmetry of H_c in Eq. (2). For $\phi = 0$ or π, t_R is real ($t_R = \pm|t_R|$). One can then define a parity operator $\mathcal{P}$ that exchanges QD-2 and QD-3 (with an additional sign factor for $\phi = \pi$ that absorbs the phase) and the time-reversal operator $\mathcal{T}$ as complex conjugation, $\mathcal{T}i\mathcal{T}^{-1} = -i$. Under these definitions, one can verify the pseudo-Hermiticity relation $(\mathcal{PT})H_c(\mathcal{PT})^{-1} = H_c^\dagger$. For small γ, the Hamiltonian satisfies this generalized $\mathcal{PT}$ symmetry and its eigenvalues remain real. Once γ exceeds the critical value γ_{c1}, the eigenvalues become complex, signaling a real-to-complex spectral transition induced by generalized $\mathcal{PT}$-symmetry breaking.

For $\phi = \pi/2$, Eq. (17) changes to $\omega^3 - A\omega - B_i = 0$ with $B_i = 2i\gamma|t_L t_R|$, and the discriminant becomes $\Delta = -\gamma^2|t_L t_R|^2 - \frac{1}{27}\left(|t_L|^2 + |t_R|^2 + t_c^2 - \gamma^2\right)^3$. Degenerate roots, i.e., a higher-order EP, appear when $\Delta = 0$, which gives

$$\gamma_{c2}^2 - 3\left(\gamma_{c2}|t_L t_R|\right)^{2/3} = |t_L|^2 + |t_R|^2 + t_c^2. \quad (19)$$

Equation (19) shows that smaller values of $|t_L|$ and $|t_R|$ facilitate the formation of the higher-order EP. The physical reason is as follows. At $\phi = 0.5\pi$, the phase difference between t_L and $t_R e^{i\phi}$ breaks the mirror symmetry of the ring completely, and the nonreciprocal coupling γ induces an effective circulating interference along the closed loop formed by the three QDs. As γ increases, the competing interference paths pull the real and imaginary parts of all three eigenenergies together. At the critical value γ_{c2}, the three eigenstates coalesce into a single eigenstate associated with a 3×3 Jordan block. Physically, this resembles coherent synchronization in a three-mode ring cavity: at the critical γ, the phase relations among the three localized states satisfy a fully constructive-interference condition, so that both their energies and their spatial distributions collapse into a single mode.

B. Transmission spectra in the symmetric case $|t_L| = |t_R|$

We now examine how the EPs manifest themselves in the transport spectrum. Figure 4 shows the transmission function $T(\omega)$ for several values of γ at different tunneling amplitudes $|t_\alpha|$ (0.2, 0.5, 1.0) and phases ϕ (0, π). All spectra exhibit pronounced Fano lineshapes with well-defined Fano antiresonances ($T(\omega) = 0$) that evolve as γ varies.

Figures 4(a) and 4(b) show the results for $|t_\alpha| = 0.2$ and $\phi = 0$. At $\gamma = 0$, the spectrum contains one Lorentzian-like peak and one Fano peak, which correspond to the real eigenlevels in the Hermitian limit, and the antiresonance is located at $\omega = t_c$. As γ increases, a new Fano resonance and an adjacent Fano antiresonance emerge in the low-energy region, which becomes increasingly asymmetric. When γ approaches the critical value $\gamma_{\rm EP} \approx 0.86$, the two antiresonances shift systematically toward $\omega \approx \pm 0.5$. At $\gamma = 0.86$, the low-energy transmission peaks merge, which indicates that the system reaches the EP, consistent with the eigenenergy spectra in Fig. 2. For $\gamma > 0.9$ [Fig. 4(b)], the low-energy transmission is strongly suppressed and the two antiresonances move closer to each other. At $\gamma = t_c$, they coalesce at $\omega = 0$ into a broad antiresonance dip. In contrast, the high-energy Fano peak is only weakly modified during this whole process, except for a slight shift toward lower energies. Figures 4(c) and 4(d) show the spectra for $\phi = \pi$. They are mirror images of those at $\phi = 0$, including the same critical value $\gamma_{\rm EP} \approx 0.86$, which directly reflects the phase-induced symmetry of the nonreciprocal coupling.

The systematic shift of the antiresonances with γ can be traced back to the structure of the nonreciprocal QD-2–QD-3 dimer. The product of the clockwise and anticlockwise interdot hoppings, $(t_c + \gamma)(t_c - \gamma) = t_c^2 - \gamma^2$, plays the role of an effective reciprocal coupling of the dimer. Increasing γ therefore weakens the bonding-antibonding splitting of the side-dot pair and pulls the associated destructive-interference points toward the band center, until they merge at $\gamma = t_c$. This mechanism is quantified by Eq. (20) below.

Figures 4(e) and 4(f) show the spectra for $|t_\alpha| = 0.5$ and $|t_\alpha| = 1.0$ at $\phi = 0$. For $|t_\alpha| = 0.5$ and $\gamma = 0$, the spectrum contains two peaks with more similar widths than in the $|t_\alpha| = 0.2$ case, while the antiresonance remains at $\omega = t_c$. As γ increases, a new Fano lineshape emerges, and two antiresonances appear near $\omega \approx \pm 1.0$ at $\gamma = 0.3$. Upon further increasing γ, the low-energy transmission peaks merge at the EP condition $\gamma = \gamma_{\rm EP} = 0.56$, during which the antiresonance positions shift only weakly. Beyond the EP, the low-energy peak is suppressed and degrades into a subpeak. The two antiresonances coalesce at $\gamma = t_c$, and for $\gamma > t_c$ the antiresonance disappears, leaving only a transmission valley. Meanwhile, the high-energy peak broadens slightly and shifts toward lower energies. For $|t_\alpha| = 1.0$ [Fig. 4(f)], the larger tunneling amplitude increases the peak separation and makes the linewidths more uniform, with a particularly narrow low-energy peak. Because no EP exists in this regime (see Fig. 2), no new Fano lineshape is formed, although a finite γ still induces an additional antiresonance. At $\gamma = 0.3$, the low-energy peak is already strongly suppressed, and the suppression intensifies with γ until the two antiresonances merge. At $\gamma = 1.2$, the

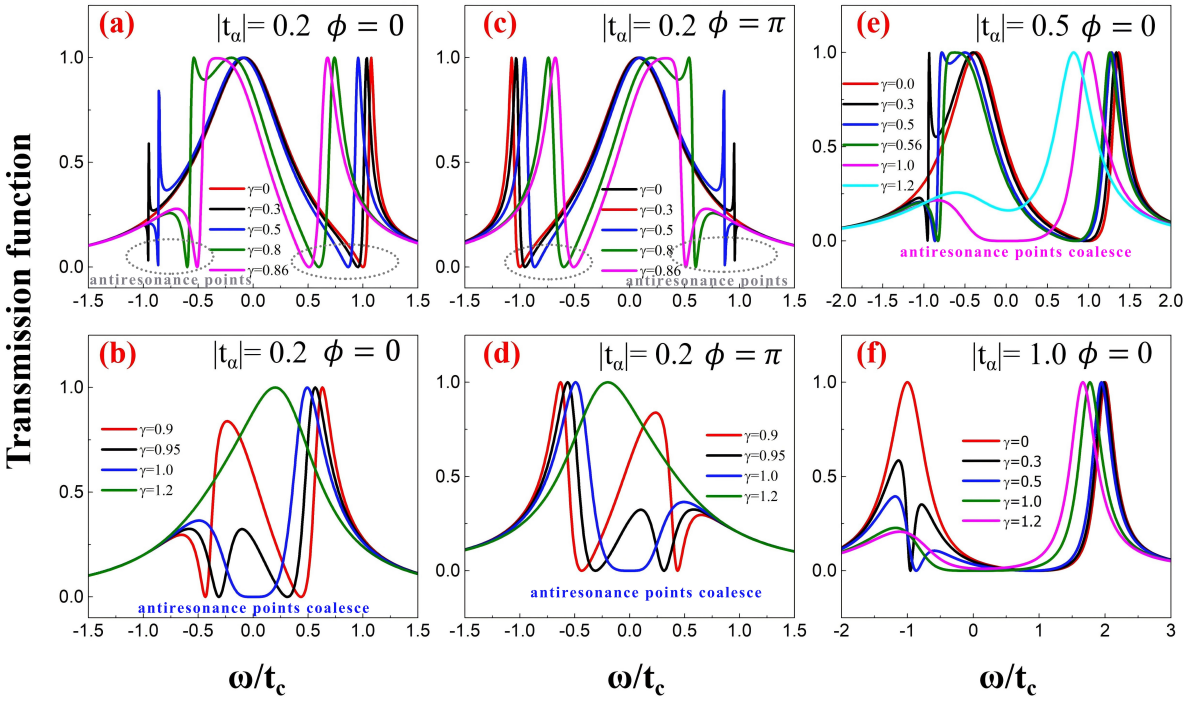


FIG. 4: Transmission function $T(\omega)$ of the TQD system for different values of the nonreciprocal coupling strength γ (indicated by the curve colors in the legends). (a),(b) $|t_\alpha| = 0.2$, $\phi = 0$; (c),(d) $|t_\alpha| = 0.2$, $\phi = \pi$; (e) $|t_\alpha| = 0.5$, $\phi = 0$; (f) $|t_\alpha| = 1.0$, $\phi = 0$. The values of γ for each curve are listed in the legends of the corresponding panels.

transmission near $\omega = 0$ shows no obvious enhancement, and only a single prominent peak survives near $\omega \approx 1.5$.

The results in Fig. 4 demonstrate that the evolution of the Fano lineshapes and antiresonances is directly correlated with the EPs in the eigenenergy spectra. The antiresonance positions shift systematically with γ and merge into a single antiresonance as γ approaches t_c. This confirms the intrinsic connection between the non-Hermitian spectral singularities and the transport properties. The $\phi = 0/\phi = \pi$ symmetry is reflected in the mirrored spectra, and the elimination of the EP at $|t_\alpha| = 1.0$ suppresses the formation of pronounced Fano antiresonances. The non-Hermitian transport characteristics are therefore efficiently tunable by $|t_\alpha|$ and ϕ.

C. Asymmetric case $|t_L| \neq |t_R|$: BIC and Fano-lineshape reversal

We next discuss the transmission when the two tunneling amplitudes differ. Figures 5(a)–5(c) show $T(\omega)$ for $|t_L| = 0.2$, $|t_R| = 0.5$, and $\phi = 0$ at several values of γ. In the Hermitian case $\gamma = 0$ (black curve), the spectrum exhibits distinct antiresonances at $\omega \approx \pm 1.0$ and two prominent Fano peaks around $\omega \approx \pm[1.0, 1.5]$. As γ increases from zero, the low-energy Fano peak moves toward higher energies and its linewidth narrows. At the critical value $\gamma = 0.72$, this Fano peak vanishes and the adjacent Fano antiresonance is simultaneously suppressed, leaving a peak-dominated spectrum. Upon a slight further increase of γ, a Fano lineshape reappears in the range $\omega \approx [-0.75, -0.5]$, as shown by the $\gamma = 0.75$ curve in Fig. 5(b). Notably, the asymmetry of this re-emerged lineshape is opposite to that for $\gamma < 0.72$. Thus, for $|t_L| \neq |t_R|$, the nonreciprocal coupling between QD-2 and QD-3 induces both a BIC and a Fano-lineshape reversal. When γ increases further, the low-energy Fano peak merges into the broad background peak, and the spectrum evolves into a two-peak structure. For example, at $\gamma = 0.9$ [Fig. 5(c)], two antiresonances appear at $\omega = \pm 0.5$ and the low-energy peak splits into two subpeaks. At $\gamma = 1.0$ (olive curve), an antiresonance emerges at $\omega = 0$ together with a broad valley, whereas the high-energy peak remains robust. At $\gamma = 1.2$ (orange curve), the high-energy peak broadens significantly and the central valley evolves into a weak plateau.

Figures 5(d)–5(f) show the corresponding results for $|t_R| = 1.0$. At $\gamma = 0$ (black curve), the spectrum exhibits antiresonances at $\omega \approx \pm 1.0$ and two Fano peaks around $\omega \approx \pm 1.5$. As γ increases to 0.8, the low-energy Fano lineshape shifts toward higher energies, while the high-energy peak remains stable. In the critical regime, e.g., at $\gamma = 0.85$ and $\gamma = 0.9$ [Fig. 5(e)], the low-energy peak broadens significantly whereas the mid-energy peak narrows. This simultaneous broadening and narrowing directly reflects the deformation of the Fano lineshape. At $\gamma = 0.92$, the mid-energy Fano peak and its adjacent antiresonance disappear simultaneously, which is the

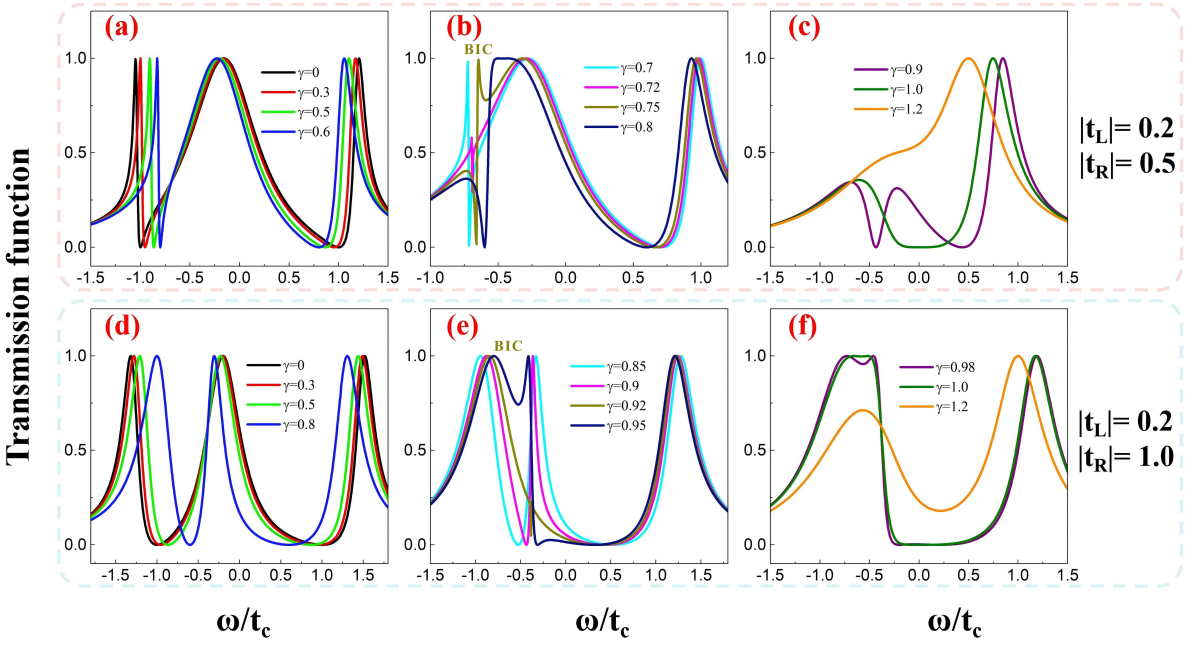


FIG. 5: Transmission function $T(\omega)$ of the TQD system for fixed $|t_L| = 0.2$ and $\phi = 0$, with $|t_R| = 0.5$ (top row, panels (a)–(c)) and $|t_R| = 1.0$ (bottom row, panels (d)–(f)), at different values of γ (indicated by the curve colors in the legends). The BIC points occur at $\gamma = 0.72$ for $|t_R| = 0.5$ and at $\gamma = 0.92$ for $|t_R| = 1.0$, in agreement with Eq. (21).

transport signature of a BIC. For $\gamma = 0.95$, a new Fano lineshape reappears with an asymmetry opposite to that for $\gamma < 0.92$, i.e., the Fano lineshape is reversed. Beyond the critical regime [Fig. 5(f)], the low-energy peaks merge into a single peak, which corresponds to an EP of the system. At $\gamma = 0.98$ (purple curve), the two low-energy peaks are on the verge of merging, and the valley between them becomes shallow. At $\gamma = 1.0$ (olive curve), they merge completely, an antiresonance with a broad valley emerges at $\omega = 0$, and the high-energy peak remains robust. At $\gamma = 1.2$ (orange curve), the high-energy peak broadens significantly and the central valley is enhanced. The overall evolution is therefore similar to that for $|t_R| = 0.5$, but a larger ratio $|t_R/t_L|$ amplifies the tunability induced by the nonreciprocal coupling, including the Fano deformation, the BIC formation, and the lineshape reversal.

To uncover the mechanisms behind the results in Figs. 4 and 5, we derive an explicit analytical expression for the transmission amplitude under the simplifying conditions $\varepsilon_j = \phi = 0$. For symmetric QD-lead couplings $\Gamma_\alpha = \Gamma$, Eq. (16) reduces to

$$\tau|_{\phi=0} = \frac{\Gamma\left[\omega^2 - (t_c^2 - \gamma^2)\right]}{\omega^3 - A\omega - B_r + i\Gamma\left[\omega^2 - (t_c^2 - \gamma^2)\right]}, \tag{20}$$

with A and B_r defined below Eq. (17). The numerator of Eq. (20) immediately identifies the antiresonance positions,

$$\omega = \pm\sqrt{t_c^2 - \gamma^2},$$

which explains the γ-driven shift of the antiresonances observed numerically: since the nonreciprocal coupling enters only through the combination $t_c^2 - \gamma^2$, increasing γ effectively weakens the side-dot dimer coupling, so the two antiresonances move toward $\omega = 0$ from $\omega = \pm t_c$. For $\gamma < t_c$, two separate antiresonance dips exist; at $\gamma = t_c$, they coalesce into one degenerate antiresonance at $\omega = 0$; for $\gamma > t_c$, the antiresonances disappear entirely. On the other hand, a pronounced decoupling effect arises when $\omega^3 - A\omega - B_r = 0$ and $\omega^2 - (t_c^2 - \gamma^2) = 0$ share one common solution, because the corresponding eigenstate then carries no spectral weight in the transmission channel. This simultaneous condition produces the BIC, characterized by the complete suppression of the Fano peak. Combining the two algebraic constraints yields the critical nonreciprocal coupling

$$\gamma_{\rm BIC} = \frac{\left||t_L|^2 - |t_R|^2\right|}{|t_L|^2 + |t_R|^2}\, t_c. \tag{21}$$

This result can also be derived from the eigenstate perspective. A BIC emerges when a localized eigenstate of the isolated TQD core has zero amplitude on QD-1 ($c_1 = 0$), because the leads couple exclusively to this site. For H_c with $\phi = 0$ and $\varepsilon_j = 0$, the eigenvalue equations with $c_1 = 0$ give $c_3 = -(|t_L|/|t_R|)c_2$, $\omega c_2 = (t_c + \gamma)c_3$, and $\omega c_3 = (t_c - \gamma)c_2$. Eliminating c_2 and c_3 reproduces Eq. (21), with the BIC energy

$$\omega_{\rm BIC} = -\frac{2t_c|t_L t_R|}{|t_L|^2 + |t_R|^2}. \tag{22}$$

Equations (21) and (22) reveal the physical mechanism of the BIC and the lineshape reversal. The tunneling asymmetry $|t_L| \neq |t_R|$ is a necessary condition, and the nonreciprocal coupling γ compensates for this imbalance so that destructive interference occurs exactly at QD-1, trapping the electron in the QD-2–QD-3 subspace. More precisely, the direction of the destructive interference depends on the relative magnitude of γ and $\gamma_{\rm BIC}$. For $\gamma < \gamma_{\rm BIC}$, the nonreciprocal coupling is insufficient to balance the asymmetric leakage through QD-2 and QD-3, and the transmission zero lies on one side of the Fano peak. At $\gamma = \gamma_{\rm BIC}$, the balance is exact, the peak and the antiresonance annihilate, and the state decouples from the continuum. For $\gamma > \gamma_{\rm BIC}$, the compensation is overdone, the effective interference phase changes sign (equivalently, the effective Fano parameter reverses its sign), and the transmission zero re-emerges on the opposite side of the peak. This sign reversal of the interference phase is the microscopic origin of the observed Fano-lineshape reversal. In Fig. 5, Eq. (21) gives $\gamma_{\rm BIC} = 0.72$ for $|t_R| = 0.5$ and $\gamma_{\rm BIC} = 0.92$ for $|t_R| = 1.0$ (with $|t_L| = 0.2$), in full agreement with the numerical results. Moreover, since $\gamma_{\rm BIC}$ grows with the asymmetry, a larger detuning $|t_R/t_L|$ moves the BIC to a larger γ and enhances the associated spectral reconstruction, which explains why the BIC and the lineshape reversal become more pronounced as the detuning increases.

D. Transmission signatures of the higher-order EP

Finally, we discuss the transmission spectra at $\phi = 0.5\pi$, shown in Fig. 6. According to Fig. 2, a higher-order EP emerges with increasing γ for $|t_\alpha| = 0.2$, so Figs. 6(a)–6(c) present the evolution of $T(\omega)$ in this case. The variation of γ leads to a dramatic reconstruction of the spectrum. At $\gamma = 0$, there is a dominant central resonance at $\omega = 0$ and two symmetric side peaks, and all of them reach near-perfect transmission ($T \approx 1.0$). As γ increases to 0.5 and 0.8, the lineshapes remain similar, but the peak amplitudes are progressively suppressed and the linewidths broaden, reflecting the enhanced dissipation caused by the imaginary eigenenergies in Fig. 2(e). At $\gamma = 1.0$, the central resonance is almost suppressed and only the side peaks survive with $T \approx 0.5$. At $\gamma = 1.5$, in contrast, a sharp and intense central resonance emerges ($T \approx 3.0$) while the side peaks vanish, signaling the EP-induced collapse of the spectrum into a single dominant mode. To locate the transition precisely, we plot $T(\omega)$ at $\gamma = 1.2$ in Fig. 6(c), where the system hosts the higher-order EP. The transmission collapses into an extremely narrow, delta-function-like resonance at $\omega = 0$ with an amplitude exceeding 10^2, while the transmission at all other energies is effectively zero. This extreme frequency selectivity originates from the delicate balance between coupling and dissipation at the higher-order EP, which isolates a single dominant transmission channel. The transmission function is thus highly sensitive to the higher-order EP.

Figures 6(d)–6(f) show the spectra for $|t_\alpha| = 0.5$, where no higher-order EP exists (see Fig. 2(e)). For small γ (0, 0.5, 0.8), the spectra retain a multipeak structure consisting of a central resonance and two side peaks, but they are more sensitive to γ: whereas $\gamma = 0$ yields near-unity transmission, increasing γ suppresses the peaks to $T \approx 0.3$ at $\gamma = 0.8$ and removes the central peak. At $\gamma = 1.0$, the central resonance vanishes entirely, leaving only the side peaks with $T \approx 0.2$. At $\gamma = 1.5$, a broad transmission plateau ($T \approx 0.45$) forms in the central frequency range. This plateau can be attributed to the merging of the two side peaks, as corroborated by the $\gamma = 1.2$ result in Fig. 6(f): the spectrum there shows a double-resonance structure with symmetric peaks at $\omega = \pm 1.0$ ($T \approx 0.2$) and a transmission minimum at $\omega = 0$ ($T \approx 0.05$), in stark contrast to the single central resonance found for $|t_\alpha| = 0.2$. This comparison demonstrates that increasing $|t_\alpha|$ suppresses the higher-order EP and shifts the dominant transport mechanism to multi-resonance-mediated transmission.

The phenomena in Fig. 6 can be understood analytically. Setting $\phi = 0.5\pi$ in Eq. (16) with $\Gamma_\alpha = \Gamma$ gives

$$\tau|_{\phi=0.5\pi} = \frac{\Gamma\left[\omega^2 - (t_c^2 - \gamma^2)\right]}{\omega(\omega^2 - A) - 2i\gamma|t_L t_R| + i\Gamma\left[\omega^2 - (t_c^2 - \gamma^2)\right]}. \tag{23}$$

The symmetry of $T(\omega) = |\tau|^2$ about $\omega = 0$ is immediately evident from Eq. (23), and the antiresonances are located at $\omega = \pm\sqrt{t_c^2 - \gamma^2}$, in excellent agreement with the numerical results. Beyond these features, we note that the higher-order EP manifests itself in the complex eigenenergies of the TQD core, so the transmission spectrum provides only an approximate signature of it, namely the single-peak structure at $\omega = 0$. It is therefore instructive to examine the zero-energy transmission,

$$T(0) = \frac{\Gamma^2(t_c^2 - \gamma^2)^2}{\left[\Gamma(t_c^2 - \gamma^2) + 2\gamma|t_L t_R|\right]^2}. \tag{24}$$

In the region $\gamma > t_c$, both the numerator and the denominator increase with γ, but not synchronously. Within this picture, the higher-order EP arises approximately at $\gamma_{cx} \approx \sqrt{|t_L|^2 + |t_R|^2 + t_c^2}$. At the same time, the imaginary part of the denominator of $\tau|_{\phi=0.5\pi}$ attains its maximum under the condition $\Gamma_{cx} = \frac{2|t_L t_R|}{|t_L|^2+|t_R|^2}\sqrt{|t_L|^2 + |t_R|^2 + t_c^2}$. Since the amplitude of the transmission function results from the combined contributions of the real and imaginary parts of the denominator of τ, and since $\gamma_{cx} < \gamma_{c2}$, the condition $\Gamma < \Gamma_{cx}$ is required to resolve the higher-order EP as a maximum of $T(\omega)$ at $\omega = 0$. This analysis explicitly establishes the correspondence between the higher-order EP and the transmission characteristics.

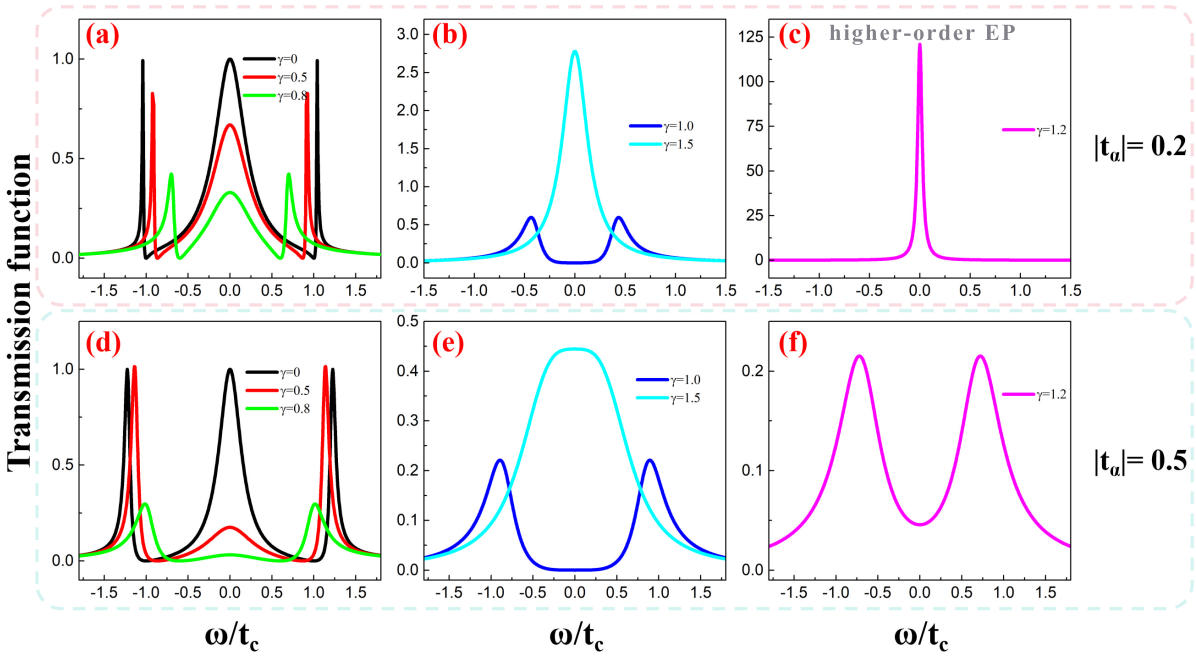


FIG. 6: Transmission function $T(\omega)$ at $\phi = 0.5\pi$ for two tunneling amplitudes: $|t_\alpha| = 0.2$ (top row, panels (a)–(c)), where a higher-order EP exists, and $|t_\alpha| = 0.5$ (bottom row, panels (d)–(f)), where no EP exists. The values of γ for each curve are indicated in the legends.

IV. SUMMARY

In summary, we have investigated the eigenenergy spectra and quantum transport of a TQD system with nonreciprocal couplings between the two side QDs. For $\phi = n\pi$, increasing the nonreciprocal coupling strength γ breaks the generalized $\mathcal{PT}$ symmetry, and a smaller γ favors EP formation when the side QDs are weakly coupled to the main-channel QD; such weak coupling also induces a higher-order EP at $\phi \neq n\pi$. In the transport spectra, nonreciprocal couplings modulate the Fano lineshapes by shifting the antiresonances, through the effective dimer coupling $\sqrt{t_c^2 - \gamma^2}$, and by inducing Fano deformation when γ meets the EP condition. For detuned main-channel-to-side-QD couplings, the nonreciprocal coupling triggers a BIC and a Fano-lineshape reversal, whose microscopic origin is the sign reversal of the interference phase once γ crosses the analytical condition $\gamma_{\rm BIC}$ in Eq. (21). At $\phi = 0.5\pi$, the higher-order EP gives rise to an extremely narrow, giant zero-energy resonance, which realizes a highly frequency-selective nonreciprocal switch. These results clarify the pivotal role of nonreciprocal couplings in regulating quantum transport in TQD structures and establish explicit connections among $\mathcal{PT}$-symmetry breaking, EPs, Fano dynamics, and BIC formation.

Acknowledgments

This work was financially supported by the Liaoning Revitalization Talents Program (Grant No. XLY-C1907033), the Natural Science Foundation of Liaoning Province (Grant No. 2023-MSLH-218), the Project of Liaoning Provincial Department of Education (Grant No. LJ212411632020), and the Fundamental Research Funds for the Central Universities (Grant No. N2405001).

Data Availability

The data supporting this study's findings are available within the article. Additional raw images and processed data are available from the corresponding author upon reasonable request.

[1] Bender C M and Boettcher S 1998 *Phys. Rev. Lett.* **80** 5243
[2] Li J R, Zhang L L, Cui W B and Gong W J 2022 *Phys. Rev. Research* **4** 023009
[3] Zhu B, Lü R and Chen S 2014 *Phys. Rev. A* **89** 062102
[4] Kawabata K, Ashida Y, Katsura H and Ueda M 2018 *Phys. Rev. B* **98** 085116
[5] Jangjan M, Li L, Foa Torres L E F and Hosseini M V 2024 *Phys. Rev. B* **109** 205142
[6] Li A D, Wei H, Cotrufo M, Chen W J, Mann S, Ni X,

Xu B C, Chen J F, Wang J, Fan S H, Qiu C W, Alù A and Chen L 2023 *Nat. Nanotechnol.* **18** 706
[7] Guo A, Salamo G J, Duchesne D, Morandotti R, Volatier-Ravat M, Aimez V, Siviloglou G A and Christodoulides D N 2009 *Phys. Rev. Lett.* **103** 093902
[8] Özdemir Ş K, Rotter S, Nori F and Yang L 2019 *Nat. Mater.* **18** 783
[9] Stegmaier A, Imhof S, Helbig T, Hofmann T, Lee C H, Kremer M, Fritzsche A, Feichtner T, Klembt S, Höfling S, Boettcher I, Fulga I C, Ma L, Schmidt O G, Greiter M, Kiessling T, Szameit A and Thomale R 2021 *Phys. Rev. Lett.* **126** 215302
[10] Lu L, Joannopoulos J D and Soljačić M 2014 *Nat. Photon.* **8** 821
[11] Li Y D, Fan C X, Hu X Y, Ao Y T, Lu C C, Chan C T, Kennes D M and Gong Q H 2022 *Phys. Rev. Lett.* **129** 053903
[12] Ozawa T, Price H M, Amo A, Goldman N, Hafezi M, Lu L, Rechtsman M C, Schuster D, Simon J, Zilberberg O and Carusotto I 2019 *Rev. Mod. Phys.* **91** 015006
[13] Guo C X, Liu C H, Zhao X M, Liu Y and Chen S 2021 *Phys. Rev. Lett.* **127** 116801
[14] Xu K, Zhang X, Luo K, Yu R, Li D and Zhang H 2021 *Phys. Rev. B* **103** 125411
[15] Zeng Q B and Lü R 2022 *Phys. Rev. B* **105** 245407
[16] Deng T S and Yi W 2019 *Phys. Rev. B* **100** 035102
[17] Li J R, Zhang L L, Zhao C H, Zhang S F, Zhu Y L and Gong W J 2024 *Phys. Rev. B* **109** 165407
[18] Yang Z, Zhang K, Fang C and Hu J 2020 *Phys. Rev. Lett.* **125** 226402
[19] Helbig T, Hofmann T, Imhof S, Abdelghany M, Kiessling T, Molenkamp L W, Lee C H, Szameit A, Greiter M and Thomale R 2020 *Nat. Phys.* **16** 747
[20] Yao S and Wang Z 2018 *Phys. Rev. Lett.* **121** 086803
[21] Yokomizo K and Murakami S 2019 *Phys. Rev. Lett.* **123** 066404
[22] Li J R, Jiang C, Su H, Qi D, Zhang L L and Gong W J 2024 *Front. Phys.* **19** 33204
[23] Hu Y M, Wang H Y, Wang Z and Song F 2024 *Phys. Rev. Lett.* **132** 050402
[24] Song F, Yao S and Wang Z 2019 *Phys. Rev. Lett.* **123** 246801
[25] Kawabata K, Okuma N and Sato M 2020 *Phys. Rev. B* **101** 195147
[26] Liu S, Shao R, Ma S, Zhang L, You O, Wu H, Xiang Y J, Cui T J and Zhang S 2021 *Research* **2021** 5608038
[27] Li R, Wang W, Kong X, Lv B, Jia Y, Tao H, Li P and Liu Y 2025 *Front. Phys.* **20** 044204
[28] Zou D, Chen T, He W, Bao J, Lee C H, Sun H and Zhang X 2021 *Nat. Commun.* **12** 7201
[29] Lin Z, Song W, Wang L W, Xin H, Sun J, Wu S, Huang C, Zhu S, Jiang J H and Li T 2024 *Phys. Rev. Lett.* **133** 073803
[30] Zhao E, Wang Z, He C, Poon T F J, Pak K K, Liu Y J, Ren P, Liu X J and Jo G B 2025 *Nature* **637** 565
[31] Zhang L L, Zhan G H, Yu D Q and Gong W J 2018 *Superlattices Microstruct.* **113** 558
[32] Zhang L L and Gong W J 2017 *Phys. Rev. A* **95** 062123
[33] Lourenço J A S, Eneias R L and Pereira R G 2018 *Phys. Rev. B* **98** 085126
[34] Kulkarni V M, Gupta A and Vidhyadhiraja N S 2022 *Phys. Rev. B* **106** 075113
[35] Zhu B, Lü R and Chen S 2015 *Phys. Rev. A* **91** 042131
[36] Li X S, Huang P P, He J, Zhang L L and Gong W J 2020 *Opt. Express* **28** 8560
[37] Zhang L L, Zhan G H, Li Z Z and Gong W J 2017 *Phys. Rev. A* **96** 062133
[38] Jin L, Zhang X Z, Zhang G and Song Z 2016 *Sci. Rep.* **6** 20976
[39] Parkavi J R, Chandrasekar V K and Lakshmanan M 2021 *Phys. Rev. A* **103** 023721
[40] Isobe H and Nagaosa N 2023 *Phys. Rev. B* **107** L201116
[41] Geng H, Wei J Y, Zou M H, Sheng L, Chen W and Xing D Y 2023 *Phys. Rev. B* **107** 035306
[42] Haldane F D M and Raghu S 2008 *Phys. Rev. Lett.* **100** 013904
[43] Martínez-Strasser C, Herrera M A J, García-Etxarri A, Palumbo G, Kunst F K and Bercioux D 2024 *Adv. Quantum Technol.* **7** 2300225
[44] Paolucci F, De Simoni G and Giazotto F 2023 *Appl. Phys. Lett.* **122** 042601
[45] Ghaemi-Dizicheh H and Schomerus H 2021 *Phys. Rev. A* **104** 023515
[46] Jing Y Z, Xiao K W, Ma Y Q, Dou F Q and Wang W Y 2025 *New J. Phys.* **27** 033015
[47] Wang L, Jing Y Z, Xiao K W and Wang W Y 2025 *Phys. Scr.* **100** 055113
[48] Metelmann A and Clerk A A 2015 *Phys. Rev. X* **5** 021025
[49] Sounas D L and Alù A 2017 *Nat. Photon.* **11** 774
[50] Liu Y L and Lin L 2025 *Phys. Rev. A* **112** 063728
[51] Ezawa M 2019 *Phys. Rev. B* **99** 201411
[52] Hofmann T, Helbig T, Schindler F, Salgo N, Brzezińska M, Greiter M, Kiessling T, Wolf D, Vollhardt A, Kabaši A, Lee C H, Bilušić A, Thomale R and Neupert T 2020 *Phys. Rev. Research* **2** 023265
[53] Rafi-Ul-Islam S M, Siu Z B, Sahin H, Lee C H and Jalil M B A 2022 *Phys. Rev. Research* **4** 043108
[54] Zhu P, Sun X Q, Hughes T L and Bahl G 2023 *Nat. Commun.* **14** 720
[55] Du L, Liu S, Shao R, Zhang L, You O, Wu H, Xiang Y J, Cui T J and Zhang S 2025 *Phys. Rev. B* **112** 115417